Japanese Journal of
Applied Physics

REGULAR PAPER

On-chip band-stop filter using multimode waveguide Bragg grating in alumina visible-light waveguides

To cite this article: Ryota Kitagawa *et al* 2026 *Jpn. J. Appl. Phys.* **65** 02SP15

View the article online for updates and enhancements.

Japanese Journal of Applied Physics **65**, 02SP15 (2026) **REGULAR PAPER**
https://doi.org/10.35848/1347-4065/ae34b8

On-chip band-stop filter using multimode waveguide Bragg grating in alumina visible-light waveguides

Ryota Kitagawa[1*], Takuto Yamaguchi[1], Naoki Fushimi[1], Masaharu Hida[1], Tetsuya Miyatake[1], Toshiyuki Miyazawa[1], Kenichi Kawaguchi[1], Ryoichi Ishihara[2], and Shintaro Sato[1]

[1]Quantum Laboratory, Fujitsu Research, Fujitsu Limited, 10-1 Morinosato-Wakamiya, Atsugi, Kanagawa 243-0197, Japan
[2]QuTech, Delft University of Technology, Mekelweg 4, 2628 CD Delft, The Netherlands

*E-mail: kitagawa.ryota@fujitsu.com

Received November 4, 2025; revised December 17, 2025; accepted January 6, 2026; published online January 28, 2026

Efficient elimination of unwanted light while transmitting lights with desired wavelengths is crucial in integrated photonics. We demonstrate a band-stop filter in alumina low-loss visible-light waveguides that eliminates green light while transmitting red light, applicable to diamond spin-based quantum computing. The filter employing a multimode waveguide Bragg grating (WBG) where forward TE_0 and backward TE_2 modes couple strongly, exhibits single-mode red light transmission and superior green light elimination compared to conventional TE_0–TE_0 coupling. The elimination wavelength changes linearly with the WBG period, offering tunability to target unwanted green wavelengths. A minimum transmittance of 10^{-3} is achieved for $N = 10\,000$ periods. This band-stop filter is a key component for integrated photonics, especially for on-chip photonic quantum processors.

1. Introduction

In integrated photonics, filtering light depending on wavelengths is sometimes necessary.[1,2] An on-chip integrated diamond-spin quantum computer using nitrogen-vacancy centers (NV centers)[3–6] is one such example.[7] There, green light, typically with wavelength of 515 nm or 532 nm, is irradiated onto NV centers in diamond for charge state initialization.[8–10] On the other hand, NV centers emit red photons entangled with their spin states, typically at a wavelength of ⩾ 637 nm.[11,12] Without a band-stop filter, both red and green lights are directed to an on-chip single photon detector (SPD). The typical power of the green light is in the tens of microwatts (μW), which can damage the SPD.[8–10]Therefore, a band-stop filter to eliminate green light while transmitting red light is needed. Band-stop filters have been already realized in several visible-light waveguide platforms such as silicon nitride,[13–15] lithium niobate,[16] and polydimethylsiloxane.[17] However, to our knowledge, none have been reported for alumina visible-light waveguide platforms, which are promising for diamond spin quantum computers due to low transmission loss arising from a low refractive index.[18]

Several structures formed in on-chip photonic waveguides have realized band-stop filter. Photonic crystals have a structure of nanoscale holes on the sides of a waveguide and eliminate light due to Bragg reflection while transmitting other wavelengths.[19–21] Nevertheless, fabricating structures with small holes is challenging. Ring resonators have a structure consisting of a ring waveguide adjacent to a straight waveguide and eliminate wavelengths that are integer multiples of the ring's circumference.[22,23] While fabrication is relatively easy, it can eliminate red light. In this study, we focused on waveguide Bragg grating (WBG).[24–26] A WBG has a periodic "fishbone" structure in the waveguide and eliminates light at a wavelength satisfying the condition $\Lambda = \lambda/n_{\mathrm{eff}}/2$, and transmits other wavelengths. Here, Λ is a period of WBG, n_{eff} is an effective index, and λ is a free-space wavelength. Compared to photonic crystals, WBG offers ease fabrication.

In our scenario, WBGs face the challenge that conventional single-mode WBGs cannot be used for eliminating green light while transmitting red light as a single-mode wave with low loss. This is because the green lights propagate as multimode waves. Instead, we focused on multimode WBG,[27–31] which utilizes strong coupling between forward TE_0 and backward higher order modes. The idea has been demonstrated for coupling from TE_0 to TE_1[27–29] or TE_2[30–32] modes. Among them, coupling to the TE_2 mode has been investigated in telecom wavelengths with periodic nano hole structures,[30,31] which requires process techniques with high precision, or a "fishbone" structure,[32] whose merit is ease fabrication. In contrast, we realize a multimode WBG utilizing TE_0 to TE_2 coupling in visible wavelengths with a "fishbone" structure.

We demonstrate a band-stop filter on an alumina waveguide platform using a multimode WBG, which transmits red light in a single-mode with low loss and eliminates green light, reported in the International Conference on Solid State Devices and Materials (SSDM).[33] This study further extends our research by additional numerical calculation and comparison between experimental and simulated results. Strong coupling between forward TE_0 and backward TE_2 modes eliminates green light more effectively than TE_0-to-TE_0 coupling by an order of magnitude, as expected from simulations. The elimination wavelength changed linearly with the WBG period. This change indicates that the elimination wavelength can be adjusted to target specific green light wavelengths by tuning the WBG period. The minimum transmittance of green light is 10^{-3} at $N = 10\,000$. This band-stop filter is useful for integrated photonics, especially for quantum computers using diamond spins.

2. Experimental methods

2.1. Multimode waveguide Bragg grating

For red lights to propagate in a single-mode with low loss, the waveguide should be as wide as possible within the range that allows single-mode propagation[18]: as the waveguide becomes wider, the effect of sidewall roughness on the transmission losses are mitigated. In such a wide waveguide, green light propagates as a multimode wave. Therefore, conventional single-mode WBG cannot be used.

Instead, we focused on multimode WBG.[27–29,31] Our multimode WBG eliminates multi-mode green lights using strong coupling between TE_0 and TE_2 modes, while transmitting single-mode red lights with low loss. Its structure is periodic "fishbone" in a waveguide, similar to a conventional single-mode WBG [Fig. 1(a)]. The coupling strength between forward TE-m mode and backward TE-n mode is expressed by the following equation[27,31]

$$\int \psi_m^*(x, y)\epsilon(x, y)\psi_n(x, y)dxdy. \tag{1}$$

Here, $\psi_\xi(x, y)$ is an electric field distribution of TE_ξ mode. $\epsilon(x, y)$ is a perturbation. Depending on the shape of the perturbation, coupling from the TE_0 mode to higher order mode can achieve higher coupling efficiency than conventional TE_0 to TE_0 coupling. In our design, W is 1 μm for red lights to propagate in a single-mode with low loss and ΔW is 0.26 μm, limited by fabrication stability (too long or short ΔW is unstable). In such a case, TE_0 to TE_0 coupling offers relatively smaller coupling efficiency: although the product of the first and third terms is large, small product of $\epsilon(x, y)\psi_0(x, y)$ (as the TE_0 mode has a weak electric field around the perturbation) contributes to the small coupling strength. However, TE_0 to TE_2 coupling offers higher coupling efficiency: the TE_2 mode has strong electric field around the perturbation and $\epsilon(x, y)\psi_2(x, y)$ is large, contributing strong coupling strength.

Such coupling between forward and backward waves occurs at specific wavelengths. The central elimination wavelength λ is expressed by the following equation[31]:

$$\frac{n_{\mathrm{eff0}} + n_{\mathrm{eff2}}}{2} = \frac{\lambda}{2\Lambda}. \tag{2}$$

$n_{\mathrm{eff}n}$ is the effective refractive index of the TE-n mode and Λ is the period of the WBG. To understand the wavelength condition given by Eq. (2), a band diagram is helpful. We performed a 3D plane wave expansion calculation to obtain the band diagram for our WBG [Fig. 1(c)]. The simulation model includes an under SiO_2 layer, alumina waveguide and remaining SiO_2 hardmask, whose dimensions are extracted from the SEM image [Fig. 2(a)]. The simulation assumes

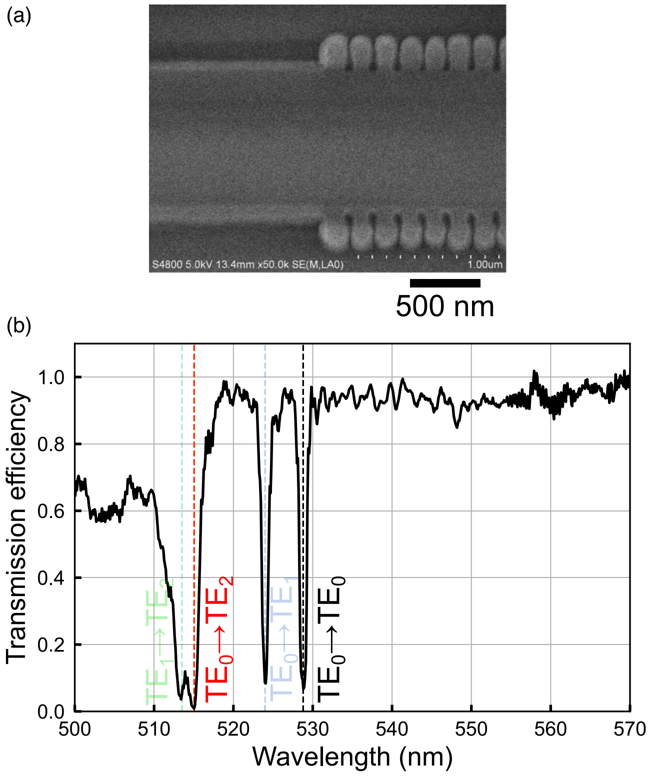

Fig. 2. (a) SEM image of WBG in alumina waveguides. (b) Measured transmission spectra of WBG with $\Lambda = 171$ nm and $N = 1000$.

that the sidewall of the waveguide is completely vertical. Figure 1(c) shows the band diagrams for the TE_0, TE_1, and TE_2 modes below the light line. TE_0 to TE_0 coupling occurs at the bandgap of the TE_0 mode [black dashed line in Fig. 1(c)]. TE_0 to TE_2 coupling occurs at the crossing point of the TE_0 and TE_2 modes in the band diagram [red dashed line in Fig. 1(c)]. At this crossing point, the actual wavenumber of the TE_0 mode (without considering folding according to Bloch's theorem) is $1/2\Lambda + k'$, and the one of the TE_2 mode is $1/2\Lambda - k'$, which satisfies Eq. (2).

Together with the band diagram calculation, we simulated the transmission spectra of the same WBG using finite-difference time-domain (FDTD) method. The simulated transmission spectra for a WBG with $N = 1000$ is shown in Fig. 1(d). The red and black dashed lines are plotted at the

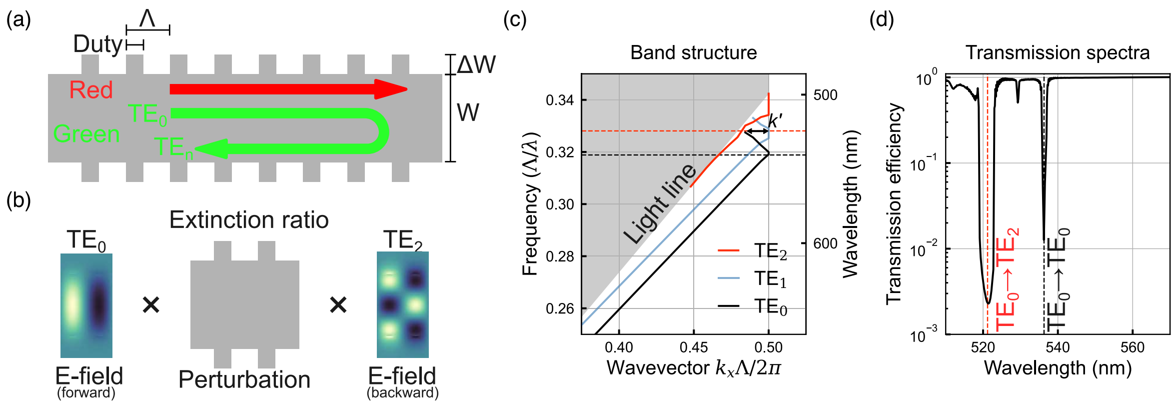

Fig. 1. Band-stop filter using multimode waveguide Bragg grating (WBG) (a) concept of band-stop filter applicable in diamond spin-based quantum computer. Red light transmits as a single mode wave whereas the green light is eliminated by strong coupling between forward TE_0 and backward TE_2 modes. (b) The terms determining extinction ratio. (c) Simulated band structure. (d) Simulated transmission spectra of WBG with $N = 1000$. Two dashed lines in (c) and (d) are shown at the same wavelengths. TE_0 to TE_2 coupling exhibits larger extinction ratio compared with TE_0 to TE_0.

same wavelengths as in Fig. 1(c). Two apparent dips appear at around 537 and 522 nm, corresponding to TE_0 to TE_0 and TE_2 coupling, respectively. The extinction ratio is 1.5×10^{-2}, 2×10^{-3}, respectively, indicating that TE_0 to TE_2 coupling realizes stronger coupling than TE_0 to TE_0 coupling by an order of magnitude.

2.2. Fabrication of WBG

We fabricated the WBG in an alumina waveguide platform using standard lithography techniques. The procedure is the same as that described in Ref. 18. An alumina layer with a thickness of 300 nm is deposited on a thermally oxidized Si substrate. An SiO_2 hardmask with a thickness of 600 nm is deposited. An electron beam resist is spin-coated and developed into the desired waveguide and WBG patterns. After SiO_2 hard mask etching, alumina etching, and resist removal, the WBG was formed in the alumina waveguide.

The structural parameters of WBG, labeled in Fig. 1(a), are determined considering expected transmission characteristics and stability in the fabrication. Λ and N are sweep parameters with ranges of 168–183 nm, 500–10 000, respectively: we aimed to observe TE_0 to TE_2 coupling at around 515–532 nm in the Λ sweep and obtain high elimination ratio in the N sweep. W is 1 μm to support single-mode propagation for 637 nm-lights. (The design value considers the pattern broadening after the fabrication.) ΔW and duty's design values were 200 nm and 40%, respectively, considering the stability of fabrication: an extreme design such as too long ΔW or too small duty is unstable.

The SEM image of the fabricated WBG is shown in Fig. 2(a). Periodic "fishbone" structures are created. Period Λ is 171 nm, the same as the designed value. ΔW and duty are 264 nm and 76%, respectively and have a distribution of approximately ±11 nm, ±10%, respectively, measuring from the SEM image. These distributions have negative impacts on the transmission characteristics of WBG, as discussed in Sect. 3.3. Improving the homogeneity would further lower the transmittance.

3. Results and discussion

3.1. Transmission spectra of multimode WBG

We measured the transmission spectra of the fabricated WBG. A broadband light with wavelengths ranging from 500 nm to 570 nm was input to one end of the waveguide including the WBG via a polarization maintaining lensed fiber with top radius of 5 μm. The input light has a linear polarization parallel to the substrate, thus they are TE mode in the waveguide. The output light from the other end was collected via another single-mode lensed fiber with top radius of 5 μm and directed into a spectrometer. To obtain the transmission spectra of WBG, the spectra was divided by that of a waveguide without a WBG. This process removes out-of-interest wavelength-dependent factors such as the spectral distribution of the light source, the waveguide-to-fiber coupling efficiency, and the fiber transmittance.

The spectrum of a WBG with $\Lambda = 171$ nm and $N = 1000$ is shown in Fig. 2(b). The spectrum exhibits band-stop filter-like characteristics, with multiple dips at 529, 524, and 515 nm, and flat regions in >529 nm. In addition to the spectroscopic measurement, the transmittance of 637 nm red light was evaluated to be 94%, demonstrating WBG's high transmission efficiency for red light.

We discuss the origin of each dip. The dips at 529 nm and 515 nm correspond to TE_0 to TE_0 and TE_2 coupling, respectively: the band diagram in Fig. 1(c) suggests that the dip at the longest wavelength originates from TE_0 to TE_0 coupling. The dip corresponding to TE_0 to TE_2 coupling is expected to appear approximately 15 nm below that of TE_0 to TE_0 coupling. The existence of these two dips is consistent with the simulation depicted in Fig. 1(d). However, a dip that is not prominent in the simulation appears at 524 nm (the blue dashed line) and 513 nm (the green dashed line). The dip wavelength of the former (the latter) is the crossing point of TE_0 and TE_1 (TE_1 and TE_2) modes in the band diagram. Thus, this dip is attributed to coupling between them. The reason this dip is prominent only in the experimental data will be the asymmetry, required to excite TE_1 mode, arising from fabrication imperfections and a fiber-to-waveguide coupling. Still, this unexpected dip does not overlap with the wavelength of the red light intended for transmission, so it does not pose a significant problem.

Next, we discuss the elimination wavelength. The dip of TE_0 to TE_2 coupling appears at 515 nm in the experimental data but at 522 nm in the simulation. This difference can be attributed to several factors such as differences between the refractive index set in the simulation and its actual value, the omission of sidewall angles in the simulation, and imperfect calibration of the spectrometer. As shown in Fig. 3, the central elimination wavelength is adjustable; therefore, the difference between simulated and experimental values does not present a significant issue.

Finally, we discuss the transmission efficiency. The elimination ratio of TE_0 to TE_2 coupling is 8×10^{-3} whereas that for TE_0 to TE_0 is 7×10^{-2}. We successfully demonstrate stronger coupling between TE_0 and TE_2 modes than TE_0 and TE_2 modes by an order of magnitude, as expected. This elimination ratio differs from the simulated value by approximately four times. The cause of this difference will be the non-uniformity, as discussed in Sect. 3.3. A more precisely replicated periodic structure would enable the achievement of even lower transmittance.

3.2. Controlling the elimination wavelength

Adjusting the elimination wavelength to the target green light wavelength is essential. The simplest method to tune the elimination wavelength is to vary the period Λ of the WBG. Within the range where the mode profiles in Eq. (1) do not significantly change, the spectrum is expected to shift lineally with respect to Λ following Eq. (2). To validate this approach, we measured the spectra of WBGs with various Λ (Fig. 3). Figure 3(a) shows the transmission spectra for $\Lambda = 168$, 171, and 174 nm with fixed N of 1000. As Λ increased, the spectrum shifted towards longer wavelengths while preserving its shape.

The dependence of the elimination wavelength on Λ was systematically investigated. The central elimination wavelength of each dip is extracted by peak fitting using a Lorentzian function [dashed lines in Fig. 3(a)]. Although the peak shapes are not strictly Lorentzian functions, they are sufficient for extracting the center. The elimination wavelength of each dip is plotted as a function of the period Λ [Fig. 3(b)]. The points represent experimental data, and the dashed lines are linear fits. As expected, the elimination wavelength shows good agreement with the linear fit. The

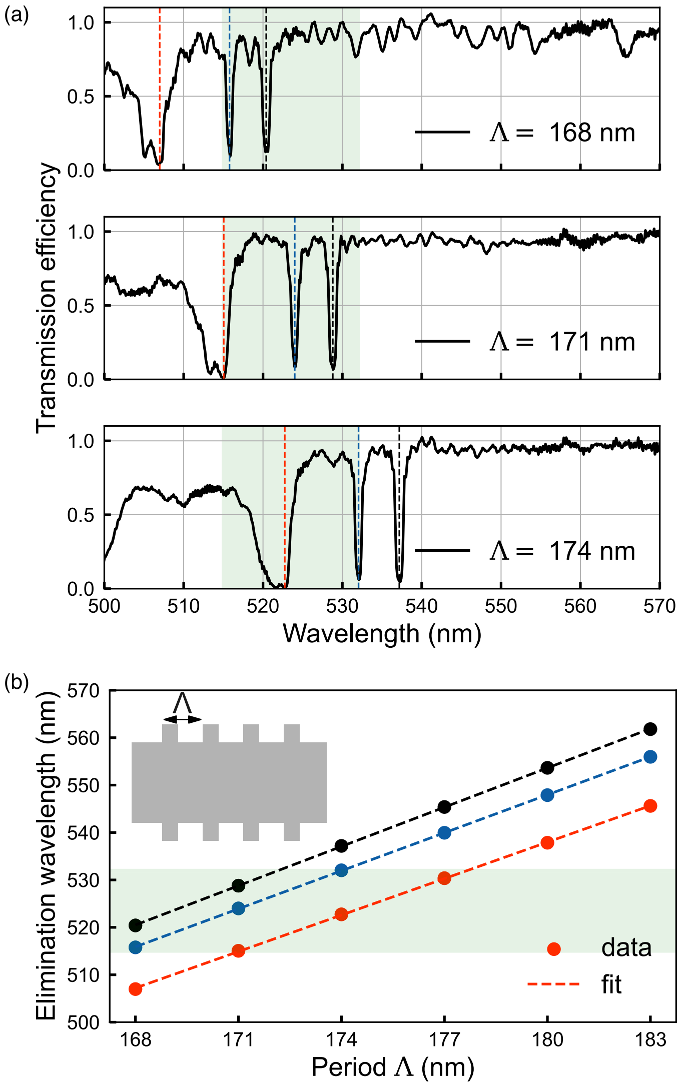

Fig. 3. Controlling the elimination wavelengths by changing the period Λ. (a) Transmission spectra of WBGs of Λ = 168, 171, 174 nm. (b) Elimination wavelength as a function of Λ. Scattering plots are ones extracted from (a). Dashed lines are linear fit.

green shaded region in Figs. 3(a), 3(b) indicates the wavelength range commonly used for green illumination of diamond color centers (515 nm–532 nm). The demonstrated tune range of the TE_0 to TE_2 coupling well covers the range of green wavelengths. These results demonstrate that the elimination wavelength can be adjusted to that of the green light by tuning the period Λ.

3.3. Improvement of elimination ratio

Improvement of elimination ratio should be realized by increasing the number of periods N. Then, we measured the transmission spectra of WBGs varying N. Figure 4(a) shows the transmission spectra of WBGs with a fixed period of $\Lambda = 171$ nm, where N is swept from 500 to 10 000. The absence of data around 513 nm for $N = 10\,000$ is due to the removal of negative values after offset subtraction. All dips exhibit a trend that as N increases, the dips become deeper, while the elimination wavelength does not significantly change.

The transmittance of each dip is examined as a function of N. The transmittance of each dip was obtained by fitting four data points around the dip with a quadratic function. We chose the quadratic fitting because just extracting the minimum value would be susceptible to noise and fitting

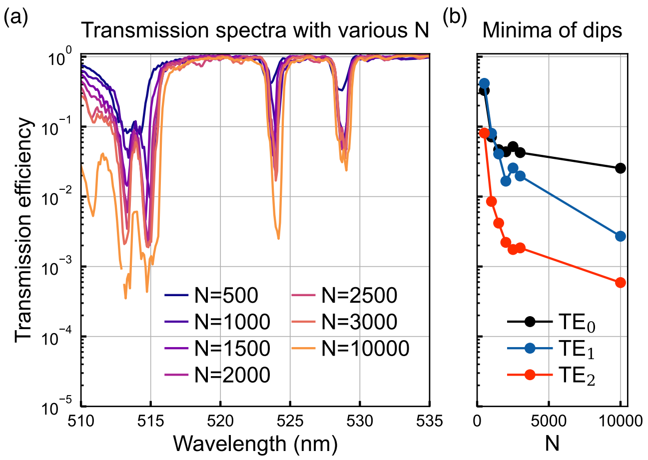

Fig. 4. (a) Transmission spectra with $N = 500$–10 000. (b) Minima of dips extracted by quadratic fitting of spectra in (a).

the entire dip with a model function is challenging. The obtained transmittance is plotted as a function of N [Fig. 4(b)]. The transmittance decreased almost monotonically with increasing N for each of dip. The minimum transmittance achieved was approximately 10^{-3} at

$N = 10\,000$. (For further reduction of the transmittance by changing ΔW, see Appendix.)

4. Conclusions

Using a multimode WBG, we demonstrated an on-chip band-stop filter capable of eliminating green light while transmitting red light. Strong coupling from TE_0 to TE_2 mode achieves a higher elimination ratio than TE_0 to TE_0 coupling by an order of magnitude. The elimination wavelength can be adjusted to that of the green lights by changing Λ. Minimum transmission was $\sim 10^{-3}$ at $N = 10\,000$. These results advance on-chip integration of diamond spin-based quantum computer.

Acknowledgments

This work was partially supported by "Advanced Research Infrastructure for Materials and Nanotechnology in Japan (ARIM)" of the Ministry of Education, Culture, Sports, Science and Technology (MEXT), proposal Numbers JPMXP1223NM0070 and JPMXP1224NM0089. We would like to thank Prof. Satoshi Iwamoto (The University of Tokyo) for the valuable discussions.

Appendix

For further improvement of the extinction ratio, employing a longer ΔW will be effective. A longer ΔW increases the product of the perturbation and the electric field distribution of TE_2 mode, thereby enhancing the coupling efficiency. We simulated the transmission spectra of WBG with ΔW ranging from 264 nm to 564 nm using 3D FDTD method (Fig. A1). $\Delta W = 264$ nm is the one measured from the SEM image in Fig. 2(a). By utilizing a longer ΔW, the dip deepens. Simultaneously, the central elimination wavelength shifts, which is attributed to the change in the effective refractive index of each mode. ΔW of 564 nm will offer an improvement of elimination ratio by approximately 10 times compared to $\Delta W = 264$ nm. However, with our current process technology, fabrication of WBG with such a loner ΔW was impossible due to issues such as resist collapse. Improving the stability of the fabrication process will enable the fabrication of WBG with longer ΔW and realize higher elimination ratio.

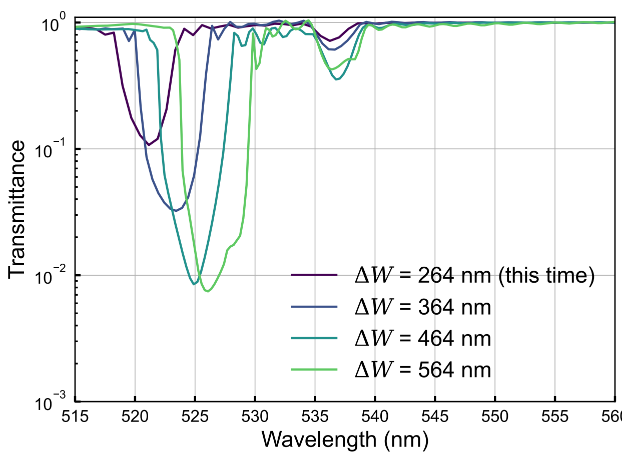

Fig. A1. Simulated transmission spectra for various ΔW. N is fixed to be 200.

ORCID iDs

Ryota Kitagawa https://orcid.org/0000-0002-8391-6019
Takuto Yamaguchi https://orcid.org/0009-0001-7181-7101

1) D. Liu, H. Xu, Y. Tan, Y. Shi, and D. Dai, Microwave Opt. Technol. Lett. **63**, 2252 (2021).
2) N. Saha, G. Brunetti, A. Di Toma, M. N. Armenise, and C. Ciminelli, Adv. Photonics Res. **5**, 2300343 (2024).
3) F. Jelezko, T. Gaebel, I. Popa, M. Domhan, A. Gruber, and J. Wrachtrup, Phys. Rev. Lett. **93**, 130501 (2004).
4) F. Jelezko, T. Gaebel, I. Popa, A. Gruber, and J. Wrachtrup, Phys. Rev. Lett. **92**, 076401 (2004).
5) M. W. Doherty, N. B. Manson, P. Delaney, F. Jelezko, J. Wrachtrup, and L. C. L. Hollenberg, Phys. Rep. **528**, 1 (2013).
6) M. H. Abobeih, Y. Wang, J. Randall, S. J. H. Loenen, C. E. Bradley, M. Markham, D. J. Twitchen, B. M. Terhal, and T. H. Taminiau, Nature **606**, 884 (2022).
7) R. Ishihara et al., 2021 IEEE Int. Electron Devices Meeting (IEDM), 2021 (IEEE, San Francisco, CA, USA), p. 14.5.1, 10.1109/IEDM19574.2021.9720552.
8) C. E. Bradley et al., npj Quantum Inf. **8**, 122 (2022).
9) C. E. Bradley, J. Randall, M. H. Abobeih, R. C. Berrevoets, M. J. Degen, M. A. Bakker, M. Markham, D. J. Twitchen, and T. H. Taminiau, Phys. Rev. X **9**, 031045 (2019).
10) M. H. Abobeih, J. Randall, C. E. Bradley, H. P. Bartling, M. A. Bakker, M. J. Degen, M. Markham, D. J. Twitchen, and T. H. Taminiau, Nature **576**, 411 (2019).
11) M. Pompili et al., Science **372**, 259 (2021).
12) K. Beha et al., Beilstein J. Nanotechnol. **3**, 895 (2012).
13) J. H. Song, T. D. Kongnyuy, B. Troia, S. S. Saseendran, P. Soussan, R. Jansen, and X. Rottenberg, OSA Contin. **2**, 1155 (2019).
14) H. Vyas and R. S. Hegde, in *Nanophotonics and Micro/Nano Optics VI*, ed. Z. Zhou et al. (SPIE, China, 2020) p. 11.
15) J. Wang, Z. Yao, and A. W. Poon, Front. Mater **2**, 34 (2015).
16) B. Desiatov, A. Shams-Ansari, M. Zhang, C. Wang, and M. Lončar, Optica **6**, 380 (2019).
17) J. S. Kee, D. P. Poenar, P. Neužil, L. Yobaş, and Y. Chen, Opt. Express **18**, 21732 (2010).
18) T. Yamaguchi et al., Jpn. J. Appl. Phys. **64**, 02SP32 (2025).
19) M. Soltani, A. Haque, B. Momeni, A. Adibi, Y. Xu, and R. K. LeeProc. SPIE 5000 (San Jose, CA), 2003ed. A. Adibi et al.,p. 257.
20) R. K. Gangwar, A. K. Pathak, and S. Kumar, Photonics **10**, 1199 (2023).
21) Q. Huang, K. Jie, Q. Liu, Y. Huang, Y. Wang, and J. Xia, Opt. Express **24**, 20542 (2016).
22) P. Xing, G. F. R. Chen, X. Zhao, D. K. T. Ng, M. C. Tan, and D. T. H. Tan, Sci. Rep. **7**, 9101 (2017).
23) S. Mandal, K. Dasgupta, T. K. Basak, and S. K. Ghosh, Opt. Commun. **264**, 97 (2006).
24) H. Saghaei, P. Elyasi, and B. J. Shastri, J. Appl. Phys. **132**, 064501 (2022).
25) W. Zhang and J. Yao, Nat. Commun. **9**, 1396 (2018).
26) R. Cheng and L. Chrostowski, J. Light. Technol. **39**, 712 (2021).
27) J. M. Castro, D. F. Geraghty, S. Honkanen, C. M. Greiner, D. Iazikov, and T. W. Mossberg, Appl. Opt. **45**, 1236 (2006).
28) D. Liu, H. Wu, and D. Dai, J. Lightwave Technol. **37**, 2217 (2019).
29) M. Barona-Ruiz, C. Pérez-Armenta, A. Ortega-Moñux, G. Wangüemert-Pérez, Í. Molina-Fernández, P. Cheben, and R. Halir, Opt. Express **30**, 38930 (2022).
30) S. Wu, J. Hao, Z. Zhao, and X. S. Yao, Opt. Express **29**, 27640 (2021).
31) Z. Xu, B. Tu, and H. Liu, Opt. Express **32**, 13156 (2024).
32) X. Chen, X. Kang, Y. Gan, X. Zhang, N. Wang, Y. Zhu, J. Zhang, and X. Gan, Opt. Express **33**, 35385 (2025).
33) R. Kitagawa, T. Yamaguchi, N. Fushimi, M. Hida, T. Miyatake, T. Miyazawa, K. Kawaguchi, R. Ishihara, and S. Sato, Ext. Abstr. of the 2025 Int. Conf. on Solid State Devices and Materials (SSDM), G–5-012025, 10.7567/SSDM.2025.G-5-01.